



Rupture Disc Monitoring Using Electro-mechanical Impedance (EMI): A Feasibility Study

Dongdong Chen¹ · Xiaoyu Xu¹ · Honglie Xuan² · Bin Guo³ · Linsheng Huo⁴ · Jianliang Yu^{5,6}

Received: 23 December 2022 / Accepted: 6 June 2023 / Published online: 23 June 2023
© The Author(s), under exclusive licence to Springer Science+Business Media, LLC, part of Springer Nature 2023

Abstract

Rupture disc is widely used in pressure vessels. To prevent catastrophic overpressure in pressure vessels, it is vital to replace the rupture disc before its premature failure. This paper presents a systematic and comprehensive study of EMI-based rupture disc monitoring. A PZT actuator-driven one-degree-of-freedom spring-mass-damper model was established, and the analytical result shows that the EMI is determined by the local stiffness of the coupled structures. Since the stiffness of a clamped rupture disc is mainly controlled by its inner pressure, the operating conditions can therefore be estimated by measuring the impedance signal. To verify this finding, a numerical model is built and the simulation result shows that as the pressure increases, the resonant frequencies of the impedance signals decrease gradually. Conventional simple domed rupture discs were tested for validation experiments. Three replacement matrices (RM_s) were proposed and compared based on the root mean square deviation (RM_{RMSD}), mean absolute percentage deviation (RM_{MAPD}), and correlation coefficient deviation (RM_{CCD}). The optimum rupture disc update time can be determined by the calculation of the RM_{MAPD} . In addition, the influences of temperature variation on EMI signals were investigated and a temperature compensation method was proposed. Experimental results demonstrated that EMI-based rupture disc monitoring is an effective method of preventing the occurrence of catastrophic overpressure accidents in pressure vessels.

Keywords EMI · PZT · Rupture disc · Burst monitoring · Replacement matrices

1 Introduction

A pressure vessel is an enclosed device that holds the gas/liquid and is subjected to a certain pressure [1, 2]. Due to its unique features of the operating environment and storage medium, overpressure bursting accidents are prone to occur. Therefore, to prevent the occurrence of pressure vessel overpressure accidents, overpressure relief devices need to be installed on the pressure vessel to keep the pressure inside the pressure vessel within a safe range utilizing safety relief technology. Specifically, the safety valve [3] and the rupture disc [4] are two typical pressure relief devices. Due to its advantages of large pressure relief area, rapid pressure relief speed, high-pressure sensitivity, and good corrosion resistance, rupture disc has been widely used in the pipeline system in chemical and petrochemical industries for more than 100 years. The rupture disc is a non-reclosing emergency pressure relief device, actuated by pressure differential. It is also a safety relief device that is composed of a rupture disc, clamping device, and other components. When the pressure

✉ Linsheng Huo
lshuo@dlut.edu.cn

✉ Jianliang Yu
yujianliang@dlut.edu.cn

¹ College of Civil Engineering, Nanjing Forestry University, Nanjing 210037, Jiangsu, China

² Hangzhou Applied Acoustics Research Institute, Hangzhou 310023, Zhejiang, China

³ Guangzhou Metro Design and Research Institute Co., Ltd., Guangzhou 510010, Guangdong, China

⁴ State Key Laboratory of Coastal and Offshore Engineering, Dalian University of Technology, Dalian 116023, Liaoning, China

⁵ School of Chemical Engineering, Dalian University of Technology, Dalian 116023, Liaoning, China

⁶ Dalian Duda Technology Safety System, Co., Ltd., Dalian 116012, Liaoning, China

gap between the two sides of the rupture disc reaches its predetermined value at the required bursting temperature, the rupture disc is instantly triggered (ruptured or detached) and the inner fluid medium is released.

Since (i) the rupture disc must be replaced immediately when the premature bursting occurs, and the production must be suspended; (ii) the released medium may be toxic or harmful to humans and it must be disposed of appropriately to ensure that no additional safety incidents occur. Therefore, the premature failure of the rupture disc must be avoided. However, in practical application, premature failure of the rupture disc may occur [5]. As a key component of the safety relief device, it is vital to replace the rupture disc in a timely manner to ensure the safety of the pressure vessel.

Traditional methods for the service life prediction of rupture disc mainly rely on two methods, i.e., the numerical and experimental approaches. The numerical approach refers to using the finite element method to simulate the failure process of the rupture disc and predict the service life by stress intensity analysis. For the experimental approach, it means that test the rupture disc in the laboratory under specific pressure (or cycle loads). However, studies show that many factors contribute to rupture disc failure, including the structural type, arch height, internal cyclic stresses, and material [6]. Hole-slot flat rupture disc was investigated by Hu et al. [7]. In their study, the bursting pressure is linearly changed with the inner ring hole and its bursting coefficient is a constant for the same material. The processing characteristics of the grooving were carried out by Jeong et al. [8]. Mechanical properties were investigated via experimental setups and the results were compared with finite element analysis (FEA). Micro leak testing was implemented by Sudha et al. [9] to investigate the microstructural of austenitic stainless steel rupture disc under sodium-water reaction. Their study concluded that deformation twinning is not a preferred deformation mode for austenitic stainless steels. Tang et al. [10] investigated the bursting process of a conventional domed slotted rupture disc made of Inconel 600 alloy. In their study, it was observed that the deformation between the matrix and the inclusion is inconsistent and the stress concentration exists at the interface between the matrix and inclusion. More literature about bursting performance can be found in [11–14]. Although the abovementioned literatures provide the basic principles for designing reasonable and sustainable rupture disc, accurately monitoring the burst time of the rupture disc and providing promptly warnings prior to bursting remains a challenge.

As one of the smart materials [15, 16], piezoelectric materials, including piezoelectric crystal, piezoelectric ceramics, PVDF, etc., have drawn much attention in aerospace [17, 18], biomedical [19], and civil engineering [20–23]. Due to its advantages of quick response [24, 25], high sensitivity [26, 27], wide bandwidth [28, 29], and low cost, piezoceramic is capable of sensing structural dynamic responses. In addition,

piezoceramics have direct and inverse piezoelectric effects [30–32]. Specifically, the direct piezoelectric effect refers to converting mechanical energy into electrical energy, and the inverse piezoelectric effect is the opposite process [25, 33]. Therefore, piezoceramics transducers can be used as actuators or sensors [34, 35].

Electro-mechanical impedance (EMI) method is a promising structural health monitoring approach. In 1994, a one-degree-of-freedom spring-mass-damper (SMD) PZT-structure interaction EMI model was proposed by Liang et al. [36] Based on the model, when a PZT transducer is pasted on the surface of a structure, the impedance signal is governed by the output of PZT. In practice, high-frequency external excitation (> 30 kHz) is imposed on a PZT patch, inducing coordinate deformation of the host structure. By analyzing the admittance responses, the phenomenological nature of the coupled structural system can be accurately revealed. An experimental investigation of spot-welded joint monitoring using the E/M impedance technique was carried out by Giurgiutiu et al. [37]. The experimental results show that the specimen stiffness can be used as a measure of spot-weld fatigue damage. A series/parallel multi-sensing technique was proposed by Chen et al. [38]. In their research, multi-bolt looseness detection was achieved by using the multi-input–single-output (MISO) damage detection scheme. A wireless impedance sensor node was designed by Kim et al. [39] and an interface washer is utilized in a cable-anchor joint and the bolted connection models. Na et al. [40] proposed a non-destructive testing method that combined the EMI technique with an unmanned aerial vehicle to detect internal damage to civil infrastructures. More studies about structural health monitoring using EMI can be found in [41–45].

On the basis of practical needs, this study explores the novel application of using the EMI technique to monitor the working state of rupture disc theoretically and experimentally. Monitoring principles were derived based on the PZT actuator-driven one-degree-of-freedom spring-mass-damper model. Based on the model, the resonant frequencies of the coupled structure (PZT and rupture disc) under different inner air pressure were analyzed. Experiments were carried out on three conventional simple domed rupture discs. To quantitatively predict the service life of the rupture disc, three replacement matrices (RM_s), including the root mean square deviation (RM_{RMSD}), mean absolute percentage deviation (RM_{MAPD}), and the correlation coefficient deviation (RM_{CCD}), were employed and compared. The effects of temperature fluctuations on EMI signals were considered and the temperature compensation technique was proposed. The rest of the paper is structured as follows. In Sect. 2, the EMI-based monitoring principle of rupture disc was introduced. Section 3 shows the numerical simulation of the proposed approach. The experimental investigations, including the PZT transducer, rupture disc specimen, and loading setups,

are presented in Sect. 4. The defined replacement matrices based on RMSD, MPDA, and CCD are also compared in this section. Section 5 is the investigation of temperature effects. Section 6 is the discussion. Section 7 concludes the paper.

2 Principle of EMI Technique

When a PZT is coupled with the rupture disc, it can function as the actuator and sensor simultaneously. Specifically, based on the inverse piezoelectric effect, a mechanical stress/strain will be generated when an external electric field is applied. In practice, when a harmonic excitation is applied to the system, a corresponding dynamic response occurs. Due to the positive piezoelectric effect, the dynamic response can generate electric charges on the surface of PZT. By collecting the surface charges, the dynamic response of the system can be measured. Since the external excitation-induced dynamic response of the coupled system is highly related to the parameters of the monitored structure, such as the stiffness, damping, and eigenfrequency. By measuring the parameters of the coupled structures, the health state can be monitored.

Based on the one-degree-of-freedom spring-mass-damper system (SMD) model of EMI [36], the dynamic interaction between pasted PZT and the rupture disc is presented in Fig. 1. Assuming that the coupled structure is a stable linear system, the mechanical impedance of the system is the ratio of the external excitation and the corresponding dynamic response,

$$Z = \frac{f}{\dot{x}} \tag{1}$$

where Z is the impedance of the system, F is the external force exerted by PZT, \dot{x} is velocity. Often, the external force can be exerted by harmonic excitation with the following equation,

$$f(t) = F_0 \cos(\omega t) \tag{2}$$

where F_0 indicates the maximum value of external force.

The corresponding differential equation of the system is

$$m\ddot{x}(t) + c\dot{x}(t) + K_s x(t) = f(t) \tag{3}$$

where m is the mass, c represents the damping, k is stiffness, and $x(t)$ is the displacement, The mechanical impedance of the SMD system is given by

$$Z = c + m \frac{\omega^2 - \omega_n^2}{\omega} i \tag{4}$$

where $i = (-1)^{1/2}$, ω is the excitation frequency, ω_n is the resonant frequency of the SMD system with the expression

of Eq. (5)

$$\omega_n = \sqrt{K_s/m} \tag{5}$$

For the one-degree-of-freedom SMD system, we assume that the system damping can be expressed as Rayleigh damping, which is a linear combination of mass and stiffness. It can be written as

$$c = \alpha m + \beta K_s \tag{6}$$

In Eq. (6), α and β are the Rayleigh damping scale coefficients,

$$c = \frac{2g\omega_l\omega_u}{\omega_l + \omega_u} \tag{7}$$

$$\beta = \frac{2g}{\omega_l + \omega_u} \tag{8}$$

where ω_l and ω_u are the lower limit and upper limit of response frequencies.

When the resonance of the system occurs,

$$\omega_l = \omega_u = \omega_n \tag{9}$$

The Rayleigh damping scale coefficients at that frequency can be obtained

$$\alpha = g\omega_n \tag{10}$$

$$\beta = \frac{g}{\omega_n} \tag{11}$$

Substituting Eqs. (5), (6), (10), and (11) into Eq. (4) yields

$$Z = 2g\sqrt{mK_s} + (m\omega - \frac{K_s}{\omega})i \tag{12}$$

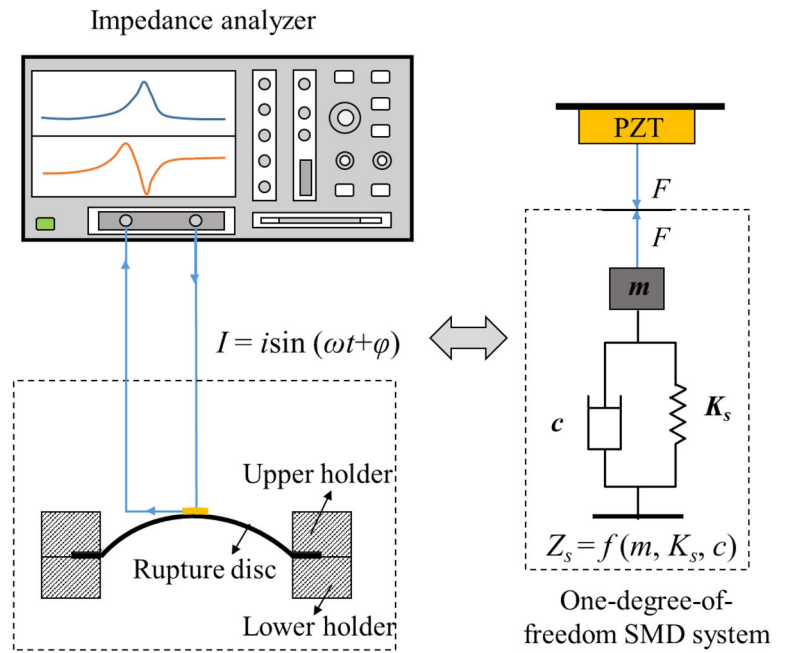
Equation (12) shows that the mechanical impedance is determined by the local stiffness of the SMD system.

According to Stepanov’s study, the variation in disk thickness has a significant effect on the rupture pressure of a disk [46]. In addition, the formula for the blasting pressure was derived theoretically by Li [47]

$$P = K\sigma(S - S_1)(D + 2K_1r) \tag{13}$$

where the $K = \frac{8w}{g(1+w^2)}$, $k_1 = (1 - \frac{w}{1+w^2})(1 + \frac{s}{2r(1+w^2)^2})$, σ is the tensile strength, S is the initial thickness of the rupture disc (unit: mm), S_1 is the thickness of the arch foot of the rupture disc, r is the radius of clamping boundary fillet, $w = H/D$ is the relative deflection, H and D are the height and bursting radius of the rupture disc, respectively. P is the bursting pressure, and g is the factor of stress concentration,

Fig. 1 A schematic representation of the one-degree-of-freedom SMD system model between a PZT and a rupture disc



which is related to the elastic stress concentration coefficient and the constitutive relationship of the groove. According to the stress–strain relationship,

$$\sigma = K_s \varepsilon \tag{14}$$

Substituting Eq. (13) into Eq. (14) gives the stiffness of the rupture disk as

$$K_s = \frac{P}{K \varepsilon (S - S_1)(D + 2K_1 r)} \tag{15}$$

Combining Eqs. (12) and (15) results in the new expression of mechanical impedance

$$Z = 2g \sqrt{m \frac{P}{K \varepsilon (S - S_1)(D + 2K_1 r)}} + (m\omega - \frac{K \varepsilon (S - S_1)(D + 2K_1 r)}{\omega})i \tag{16}$$

According to Eq. (16), for clamped rupture disc, its impedance is mainly related to the thickness, the geometry, and the material properties. Although it is difficult to directly derive the expression between the impedance of the rupture disc and its geometry parameters, the coupled mechanical impedance depends to a large degree on the working conditions of the rupture disc. By measuring the EMI signal of the coupled structure (PZT and rupture disc), the bursting signs of the rupture disc will be caught promptly to avoid premature failure.

3 Numerical Investigation

3.1 Finite Element Modeling

Equation (12) shows that the mechanical impedance of the coupled structure is related to the local stiffness of the SMD system, including the thickness, pressure, and boundary conditions of the rupture disc. However, due to the complexity of the pressure vessels, the local stiffness of the rupture disc cannot be derived directly. Therefore, in this section, the numerical simulation of the rupture disc status monitoring using the Electro-mechanical Impedance (EMI) of PZT is performed.

A free PZT wafer is modeled using COMSOL Multiphysics. The diameter of the PZT wafer (PZT-5H) is 10 mm and the thickness of the wafer is 1 mm. The stress-charge type piezoceramic equation is used for the simulation of the interaction between mechanical stress/strain and the external electric field. The material parameters of the PZT wafer are given in Table 1.

Two physical fields, namely the electrostatic field and solid mechanics, are employed and they are coupled by the piezoelectric effect multi-physical field. By doing so, the external voltage excitation will transfer to stress based on the inverse piezoelectric effect of PZT. According to Lin’s study, the resonant frequency of a PZT wafer with radial vibration mode can be expressed as [48]

$$f_r = \frac{B}{2\pi r} \sqrt{\frac{c_{11}^E}{\rho(1 - \nu_{12}^2)}} \tag{17}$$

Table 1 Parameters of PZT-5H

Elastic constants (N/m ²)	Piezoelectric constants (C/m ²)	Relative dielectric constants
$C_{11} = 1.272 \times 10^{11}$	$E_{31} = -6.623$	$\kappa_{11} = 1704.4$
$C_{12} = 8.021 \times 10^{10}$	$E_{32} = -6.623$	$\kappa_{22} = 1704.4$
$C_{22} = 1.272 \times 10^{11}$	$E_{33} = 23.240$	$\kappa_{33} = 1433.6$
$C_{13} = 8.467 \times 10^{10}$	$E_{24} = 17.035$	
$C_{23} = 8.467 \times 10^{10}$	$E_{15} = 17.035$	
$C_{33} = 1.174 \times 10^{11}$		
$C_{44} = 2.299 \times 10^{10}$		
$C_{55} = 2.299 \times 10^{10}$		
$C_{66} = 2.347 \times 10^{10}$		

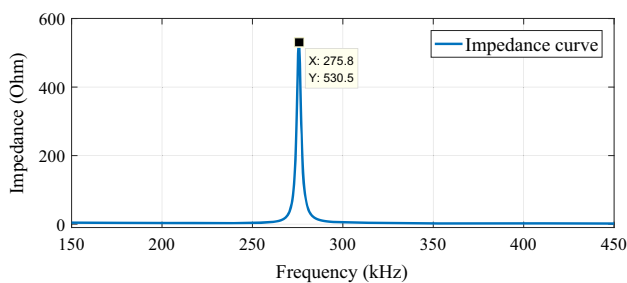


Fig. 2 The impedance signal of the simulated PZT wafer (150–450 kHz)

where f_r represents the resonance frequency. B is a constant. r is the radius of the PZT wafer. ρ denotes the density. $c_{11}^E = 1/s_{11}^E$ is elastic stiffness constant at the constant electric field in the loading direction of the PZT sensors. ν_{12} is the Poisson coefficient of the piezoelectric materials which can be written as [49]

$$\nu_{12} = -\frac{s_{12}^E}{s_{11}^E} \tag{18}$$

where s_{ij}^E is the compliance coefficient at the constant electric field.

Equation (17) indicates that once the material of the PZT is determined, the resonance and anti-resonance frequencies depend on its radius and vibrational order [50]. In our finite element model (FEM) model, the properties of the PZT include $r = 0.005$ m, $\rho = 7.5 \times 10^3$ kg/m³, $s_{11}^E = 1.65 \times 10^{-11}$ m³/N, $s_{12}^E = -4.78 \times 10^{-12}$ m³/N, $\nu_{12} = 0.29$. Substituting these parameters into Eqs. (17) and (18) yields the resonance frequency $f_r = 279.87$ kHz. Therefore, the sweep-frequency range [150 kHz, 350 kHz] is adopted in our FEM model. Figure 2 shows the impedance signal of the simulated PZT wafer. The resonant frequency of the simulated PZT wafer is 275.83 kHz, which is very close to the theoretically derived result (279.87 kHz).

Based on the PZT FEM model, the coupled structure which consists of a PZT wafer and a conventional simple domed rupture disc is established. The rupture disc is made of 360L stainless steel. Its inner diameter and thickness are 100 mm and 0.1 mm, respectively. The height of the domed rupture disc is 22 mm. The PZT is pasted on the top of the rupture disc. Since the rupture disc is made of isotropic homogeneous material and is two-dimensional axisymmetric in its cross-section view, a simplified 2D axial symmetry cross-sectional model is established, as shown in Fig. 3a. The gray dotted line at the radius of $r = 0$ is the symmetry axis. The enlarged image in Fig. 3 shows the geometric composition of the FEM model.

To accurately simulate the interaction between the PZT and rupture disc, the adhesive layer should be considered. The Young’s modulus, Poisson ratio, and density of the adhesive are 1×10^9 Pa, 0.38, and 1.2×10^3 kg/m³, respectively, which correspond to the properties of epoxy resin used in our experiments. The thickness of the adhesive layer is 0.1 mm. The PZT, adhesive layer, and rupture disc are assembled by using Form Union. Since there is almost no relative displacement between the edge of the rupture disc and the clamper [6], the boundary is set to a fixed constraint. The pressure is boundary load and it was applied in the inner boundary of the 2 D model of the rupture disc, as shown in Fig. 3b. The maximum mesh size of the model is less than 0.3 mm [51] and local grid refinement was performed in the adhesive layer. Since this research attempts to show the response of the impedance of rupture discs under excitation by voltage in the form of a frequency input, analyses in the frequency domain have been performed.

3.2 EMI Results and Analysis

Considering the actual application situations, nine testing scenarios, which are 0.2 Mpa to 1.8 Mpa with an interval of 0.2 Mpa, were simulated. It should be noticed that the loading scenarios in our simulation are consistent with the experiments detailed in Sect. 4. The simulated impedance curves are presented in Fig. 4.

As shown in Fig. 4, the impedance signals of the coupled structure changes significantly. With the pressure increase, the peak frequency shifts to the left gradually, meaning that the resonance frequency decreases with the increase of the pressure. Specifically, when the pressure is 0.2 Mpa, the peak frequency of the EMI signature is 252.1 kHz. As the pressure increase to 1.0 Mpa, the peak frequency decreases to 251.5 kHz, and its amplitude is 430.1 Ohm. The central frequency is 251.4 kHz when the pressure is 1.8 Mpa and the amplitude of the EMI signal is less than half of that value at 0.2 Mpa. According to the theoretical analysis in Sect. 2, the resonance frequency and the amplitude of the EMI signature are related to the stiffness of the rupture disc. Specifically,

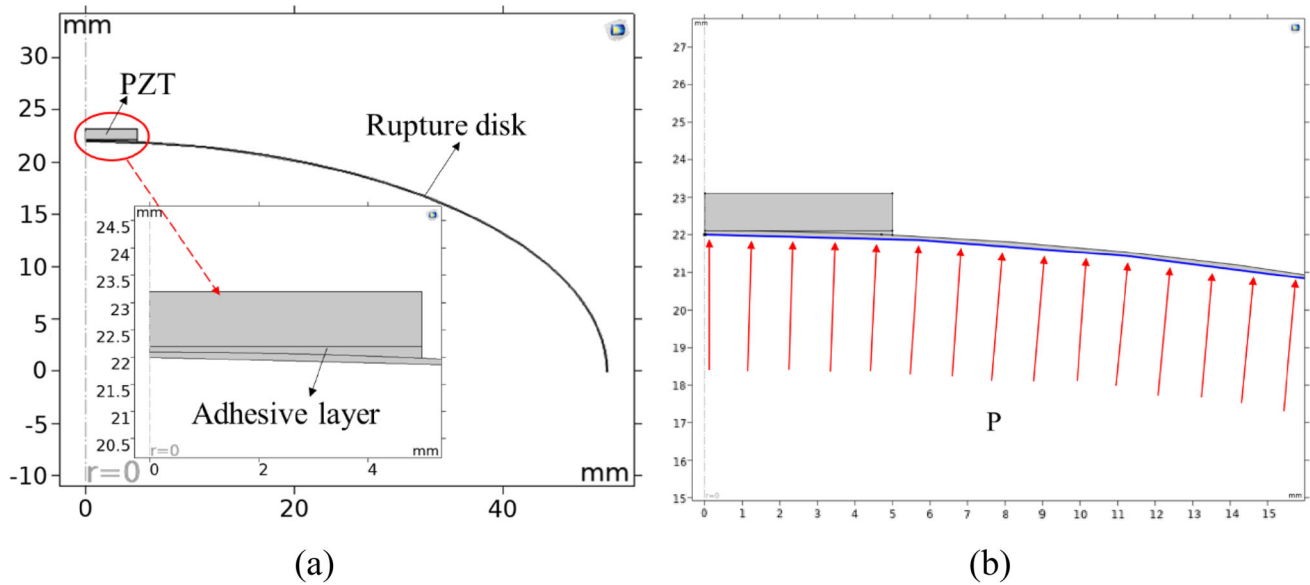


Fig. 3 2D FEM model of rupture disc **a** geometric composition, **b** inner pressure

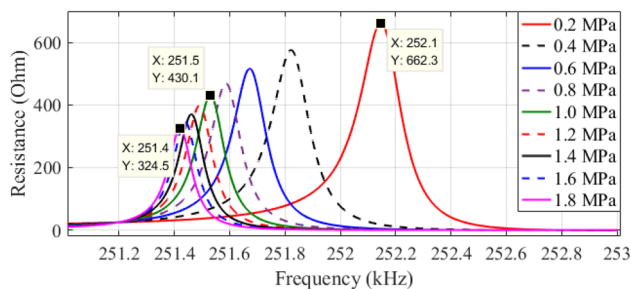


Fig. 4 The simulated impedance signatures for nine pressure scenarios

Eq. (5) shows that the resonance frequency decreases as the stiffness decreases, and Eq. (16) denotes that the thickness of the rupture disc is controlled by the inner pressure of the rupture disc. Based on the simulated results, the resonance frequency decreases gradually with the increase of inner pressure, indicating that the increase of the pressure reduces the stiffness of the rupture disc, and therefore reduces the peak frequency and the amplitude of the EMI signal. The simulated results validate the feasibility of utilizing the electromechanical impedance (EMI) principle to monitor rupture disc.

4 Experimentation

4.1 PZT Transducer, Rupture Disc, and Experimental Setup

In the experimental study, three conventional simple domed rupture discs (LP100-1.90-100) are tested. The rupture disc is manufactured by Dalian Duta Technology Safety System

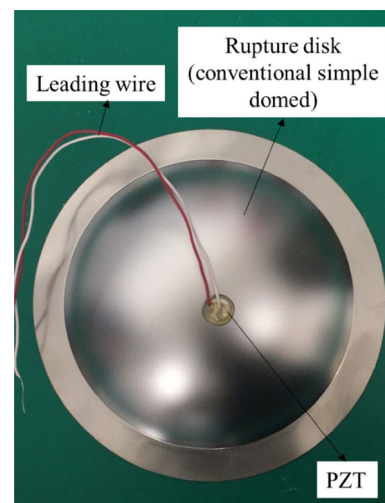


Fig. 5 Conventional simple domed rupture disc with PZT attached

Co., Ltd. Dalian, China. The rupture discs are made of 360L stainless steel with 0.1 mm thickness. The inner radius and the height are 50 mm and 22 mm, respectively. The designed burst pressure is 1.90 MPa (at 25 °C). The leading wire is connected to the commercially available PZT-5H wafer and then bonded on the top of the rupture disc by using epoxy resin. The specimen is shown in Fig. 5. The PZT transducer is produced by Baoding Hongsheng Acoustics Electron Apparatus Co. Ltd., Hebei, China. The thickness and radius of the PZT transducer are 1 mm and 5 mm, respectively.

A schematic diagram of the experimental setups is presented in Fig. 6. It mainly consists of three parts: (1) the air supply, (2) the clamp holder, and (3) the impedance analyzer. In our experiment, a multi-stage loading process is

Fig. 6 Schematic diagram of the experimental setups

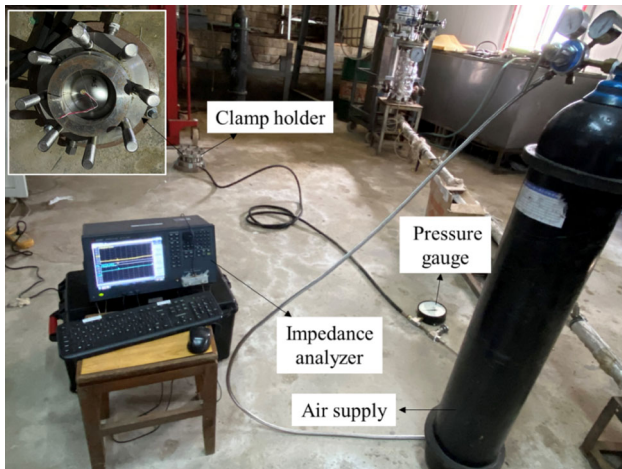
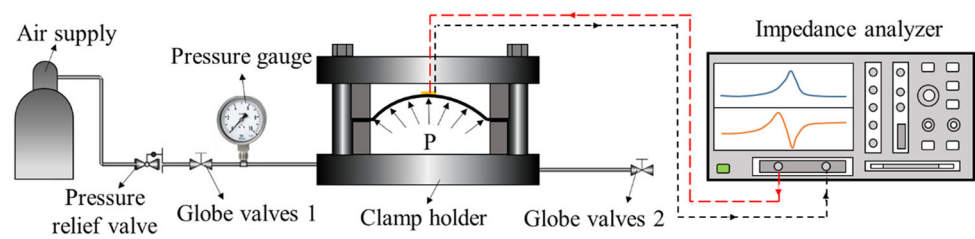


Fig. 7 Experimental device (the inserted figure is the clamp holder)

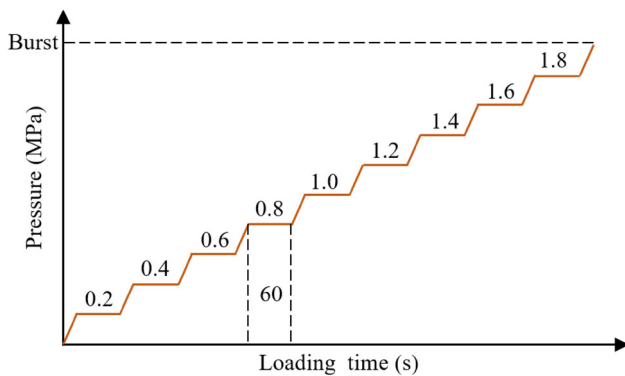


Fig. 8 Loading process of the rupture disc

used. Firstly, globe valve 2 is closed to ensure that no gas leaks out. Secondly, the air supply valve is opened to release the air pressure. The third step is to release the globe valve 1 and apply the air pressure to the inner surface of the rupture disc. Finally, the above procedure is repeated until the bursting of the rupture disc is achieved. Figure 7 is the photograph of experimental devices. In our experiment, the step-loading process was designed and implemented. As shown in Fig. 8, the pressure increment for each loading step is 0.2 MPa. The pressure holding time for each loading step is 60 s, during which the impedance of coupled structure will be recorded.

Since the design burst pressure of the conventional single-domed rupture disc is approximately 1.9 MPa, the maximum pressure at which the impedance can be recorded is 1.8 MPa.

4.2 Replacement Matrices Based on RMSD, MPDA, and CCD

To prevent catastrophic overpressure accidents, the rupture disc should be replaced before its premature failure. Although the impedance signals indicate the variation in rupture disc operating conditions, it remains unclear when to update the trend-to-failure state rupture disc. To address this issue, replacement matrices (*RM*) are proposed. To date, there are many EMI signal processing techniques. Among them, the most popular and widely used are [52]: the root mean square deviation (*RMSD*), the mean absolute percentage deviation (*MAPD*), and the correlation coefficient deviation (*CCD*).

The replacement matrices (*RM*s) based on *RMSD* [52] and *MAPD* can be written as Eqs. (19) and (20), respectively.

$$RM_{RMSD} = \sum_{i=1}^n \sqrt{\frac{[\text{Re}(Z_i^{p'}) - \text{Re}(Z_i^{p0})]^2}{[\text{Re}(Z_i^{p0})]^2}} \tag{19}$$

$$RM_{MAPD} = \sum_{i=1}^n \left| \frac{\text{Re}(Z_i^{p'}) - \text{Re}(Z_i^{p0})}{\text{Re}(Z_i^{p0})} \right| \tag{20}$$

where Z_i^{p0} and $Z_i^{p'}$ are considered as the baseline impedance signal at the healthy state and the impedance curve for the comparison, respectively. i denotes the sampling points of one impedance curve. Since the impedance signal is in complex form, in Eqs. (19) and (20), Re represents the real part of the impedance curve, which is also named resistance.

Although the *RMSD* and *MAPD* are simple and widely used, these matrices approach zero when a slight perturbation of the large impedance signal occurs, which does not provide a valid indication of the working conditions of the rupture

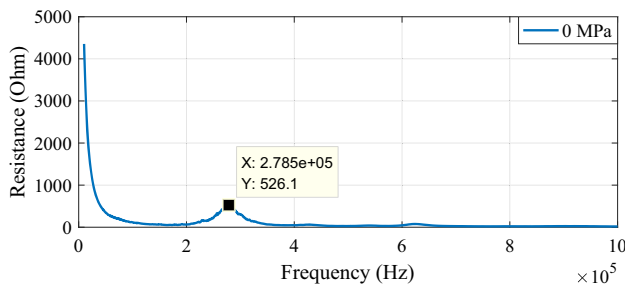


Fig. 9 The resistance curve of the coupled structure at 0 MPa

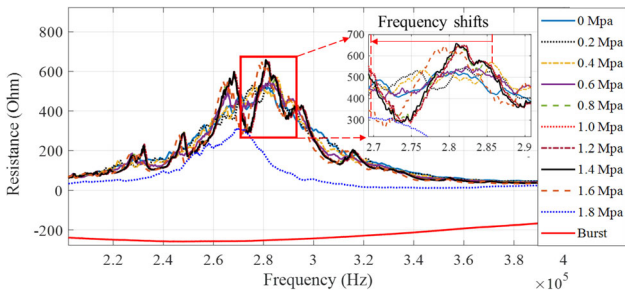


Fig. 10 The resistance curves of the coupled structure at different air pressure

disc. To address this issue, the *CCD* matrix is applied.

$$RM_{CCD} = 1 - CC, \text{ where}$$

$$CC = \frac{1}{\sigma(Z^{p'})\sigma(Z^{p0})} \sum_{i=1}^n \left\{ \left[\text{Re}(Z_i^{p'}) - \text{Re}(\bar{Z}^{p'}) \right] \times \left[\text{Re}(Z_i^{p0}) - \text{Re}(\bar{Z}^{p0}) \right] \right\} \quad (21)$$

where the \bar{Z}^{p0} and $\bar{Z}^{p'}$ signify mean values of Z^{p0} and $Z^{p'}$, respectively. $\sigma(Z^{p0})$ and $\sigma(Z^{p'})$ represent the standard deviations of Z^{p0} and $Z^{p'}$.

4.3 Experimental Results

To effectively reveal the working status of the rupture disc using the impedance signal, it is essential to determine the appropriate sweep range. Therefore, a large sweep range from 10 kHz to 1 MHz was triggered when no pressure was applied (0 MPa). Figure 9 is the real part of the impedance signal, which is also named the resistance. As shown in Fig. 10, the peak frequency of the coupled structure is 278.5 kHz and the corresponding resistance is 526.1 Ohm. By narrowing the sweep range to 200–400 kHz, the frequency shift can be observed.

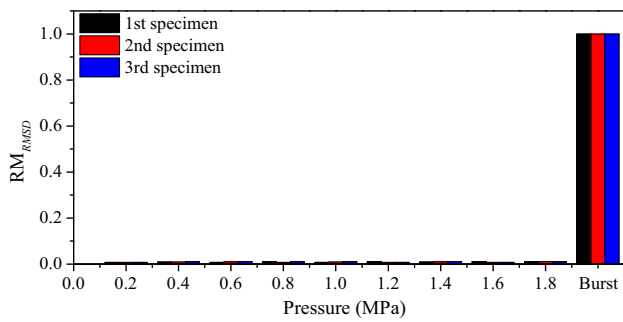
Figure 10 shows the resistance curves under different air pressure in the sweep range of 200–400 kHz. When the pressure is 0.2 MPa, the resonant frequency is 285.25 kHz. As the pressure increases to 1.4 MPa, the resonant frequency

decreases to 280.875 kHz. In addition, when the air pressure is between 0.6 and 1.4 MPa, the resonant frequency of the PZT pasted rupture disc remains constant, meaning that the impedance characteristic of the coupled structure is relatively stable. However, when the air pressure exceeds 1.4 MPa, the peak frequency shifts to the left significantly, indicating that the resonant frequency of the coupled structure decreases as the pressure increases. When the air pressure increases to 1.8 MPa, the resonant frequency and resistance are 269.5 kHz and 314.2 Ohm, respectively. The impedance curve is different from others, indicating that the impedance characteristic of the coupled structure changes significantly and the rupture disc is in a dangerous working state. In this case, the internal pressure of the rupture disc should be relieved and the rupture disc replacement is recommended.

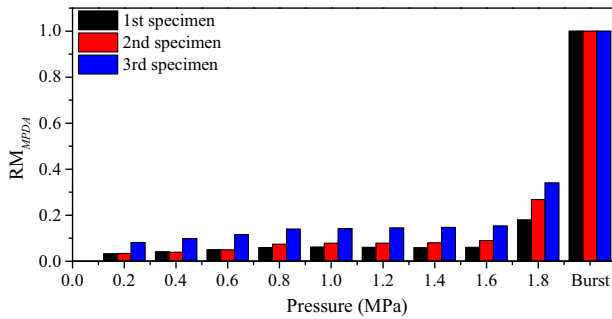
To quantitatively reveal the working states of the rupture disc, replacement matrices (*RM*s) based on *RMSD*, *MPDA*, and *CCD* are calculated and compared. As shown in Fig. 11a, the *RMSD*-based replacement matrices are almost zero when the pressure is in the range of 0–1.8 MPa. The *RM* value increases abruptly when the rupture disc bursts. Therefore, the RM_{RMSD} can not indicate the inner pressure changes of the rupture disc.

For the RM_{MPDA} in Fig. 11b, the indicator gradually increases with the increase of pressure. Specifically, when the pressure is in the range of 0–0.6 MPa, the index grows sluggishly, which means that the rupture disc is in a stable and safe working state. However, as the air pressure increases to 1.8 MPa, which is very close to its designed burst pressure, the RM_{MPDA} increases significantly, indicating a significant growth in stress in the conventional simple domed rupture disc. When the rupture disc bursts, the RM_{MPDA} is 1.0. The trends of RM_{MPDA} were generally consistent across all specimens. Based on the RM_{MPDA} , the time at which the rupture disc should be replaced can be determined. Therefore, the replacement matrix based on the *MPDA* algorithm allows a quantitative evaluation of the working condition of the rupture disc and it can be utilized as an indicator to effectively prevent catastrophic overpressure of the pressure vessel. It should be noticed that there are slight changes in the EMI signals between 0.6 and 1.4 MPa in Fig. 10 and the RM_{MPDA} remains stable during this period in Fig. 11b. This phenomenon is mainly caused by the shear lag effect, meaning that the strain of the structure cannot be fully transmitted to the piezoelectric ceramic sensor [53]. Further investigation will be carried out in our future work.

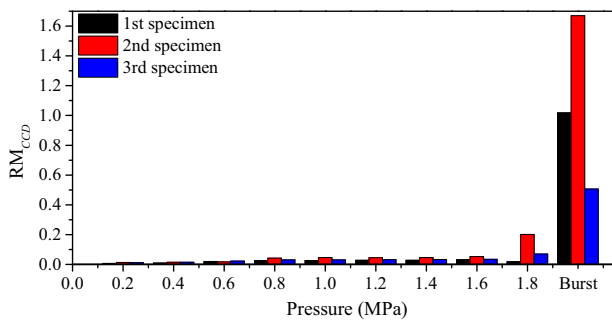
In Fig. 11c, the replacement matrices based on the *CCD* show large fluctuation among the three specimens. To be specific, before the air pressure of the first specimen reaches the maximum pressure (1.8 MPa), the RM_{CCD} remains virtually unchanged, which means that the RM_{CCD} is not sensitive to the stress variation caused by inner air pressure. When the rupture disc bursts, the index reaches its maximum value.



(a)



(b)



(c)

Fig. 11 Replacement matrices based on **a** *RMSD*, **b** *MPDA*, and **c** *CCD* algorithm

The same trend can be found in the third specimen. Only the working status of the second specimen is successfully predicted by using the RM_{CCD} . Its RM_{CCD} is less than 0.05 when the pressure is below 1.6 MPa. When the air pressure rises to 1.8 MPa, the index is 0.2, which means that there is a significant change in the working state of the rupture disc and it should be replaced for the safety of the pressure vessels. It should be noticed that the *CC* coefficients in Eq. (18) are negative for the first and second specimens due to the *CCD* algorithm, resulting in the RM_{CCD} being greater than 1.0. Generally speaking, the RM_{MPDA} shows more stable and superior performance than the RM_{RMSD} and RM_{CCD} .

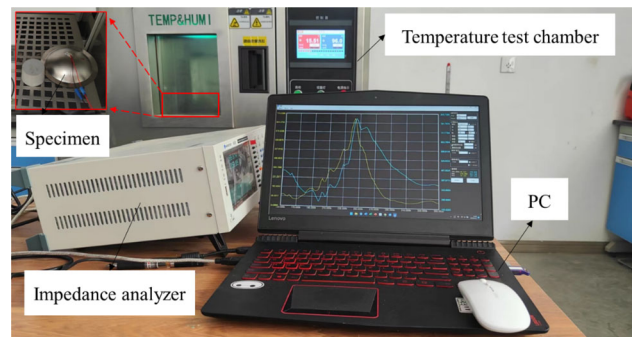


Fig. 12 Experimental setup for temperature variations investigation

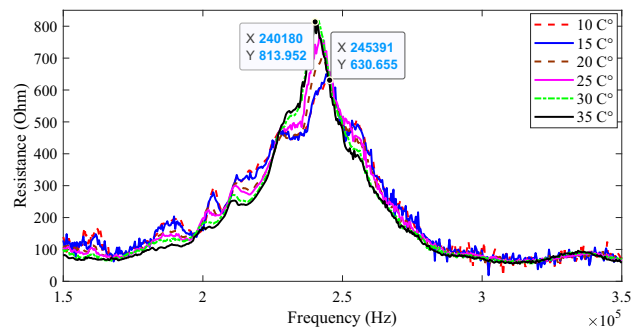


Fig. 13 The resistance curves of the coupled structure at different temperatures

5 Temperature Variations Investigation

For the in-site monitoring, the temperature of the inner medium (gas or liquid) of pressure vessels varies in real-time. Although there are temperature shielding devices in the bursting disc which protect the bursting disc from direct exposure to excessively high/low temperatures, the consequential effect of internal temperature and direct exposure to the environment should be investigated and temperature compensation technology should be considered in real-time monitoring. Figure 12 shows the experimental setup for temperature variation investigation. Specifically, the temperature change is simulated in a temperature test chamber. The range of the temperature variation is from 10 to 30 °C and the impedance signals are measured at 5 °C intervals. The resistance signals are presented in Fig. 13.

As shown in Fig. 13, the resonance frequency is 245.391 kHz at a temperature of 10 °C. When the temperature is increased to 35 °C, the resonance frequency changes to 240.18 kHz. Therefore, as the temperature increases, the resonance peak shifts to the left gradually. Using the impedance signal obtained at room temperature (25 °C) as a baseline, the frequency shifts (Δf) of the peak frequency at different temperatures against the baseline can be obtained. Table 2 shows the frequency shifts at different temperatures.

As shown in Fig. 14, the frequency shifts linearly with

Table 2 Frequency shifts at different temperatures

Temperature (°C)	10	15	20	25	30	35
Frequency shift (kHz)	3.593	2.39	0.787	0	- 0.415	- 1.618

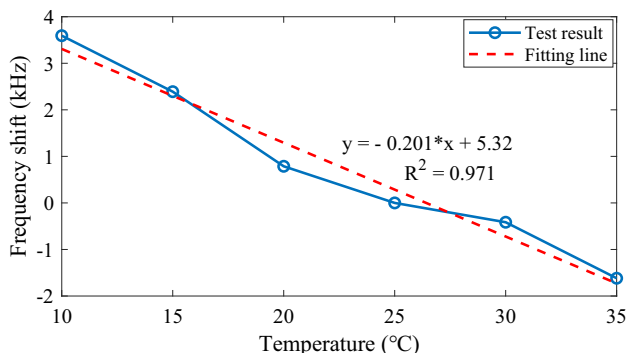


Fig. 14 Frequency shifts versus temperatures changes

the temperature changes. The linear fitting equation can be expressed as

$$y = -0.201x + 5.32 \tag{22}$$

According to Eq. (22), it can be seen that temperature does not affect the basic trend of the real impedance curve but only shifts the real impedance peak frequency. Therefore, the temperature effect can be compensated by shifting the impedance curve in the opposite direction. For the practical measurement, the baseline of the impedance curves at different temperatures should be obtained first. The temperature effect can be eliminated by compensating the difference between the measured impedance signal and the baseline curve. This will shift the curve to the right if the test temperature exceeds the reference temperature and to the left if the test temperature falls below the reference temperature. The algorithm used to compensate for temperature can be expressed as follows,

$$\text{Re}(Z_{i,T}^{p'}) = \text{Re}(Z_i^{p'}) + \text{Re}(Z_{i,T_0}^{p_0}) \tag{23}$$

where $Z_{i,T_0}^{p_0}$ is the baseline impedance signal with different temperatures, $Z_{i,T}^{p'}$ is the impedance signal with temperature compensated.

6 Discussion

The EMI-based RM_{MPDA} replacement matrix shows great potential for burst warning of the rupture disc. However, challenges still exist in adopting this approach in practical applications: (i) beyond the conventional domed bursting

disc, there are other types of bursting discs, such as the reverse domed bursting disc, flat bursting disc, graphite bursting disc, et al. The feasibility of using EMI to monitor all types of bursting discs will be investigated in our future work. It should be noticed that the reverse domed bursting disc is arched, and the convex surface is on the high-pressure side of the pressure system. Therefore, it is a challenge to bond the PZT transducer to the external surface of the reverse domed bursting disc; (ii) the marked burst pressure on the bursting disc is the arithmetic mean of the measured burst pressures when testing rupture discs from the same batch at the specified design (or permitted test) burst temperature. (iii) for most cases, the pressure vessels are large and complex. Data transmission using traditional leading wires is costly and laborious. Due to its advantages of simple layout (no leading wires), broad transmission range, and fast transmission speed, wireless impedance devices are getting more and more popular [54–56]. Future work involves the development of wireless impedance devices for rupture disc monitoring.

7 Conclusion

The main objective of this research is to develop a reliable and effective rupture disc working state monitoring approach that can prevent catastrophic overpressure accidents of pressure vessels. Monitoring principles based on Electro-mechanical impedance (EMI) of PZT transducers are proposed. A conventional simple domed rupture disc was modeled, and three conventional simple domed rupture discs (LP100-1.90-100) were experimentally tested. The main conclusions of this study can be summarized as:

- (1) Based on the EMI technique, the one-degree-of-freedom SMD system model shows that the coupled mechanical impedance of the structures (PZT transducers and the rupture disc) is determined by the local stiffness. For a clamped rupture disc, its stiffness is mainly related to the thickness, the pressure, and the boundary conditions. For a rupture disc with a fixed boundary condition, the radius is related to its inner pressure. By monitoring the mechanical impedance of the PZT and rupture disc, the working states of the rupture disc can be effectively revealed.
- (2) The numerical model shows that the peak frequency gradually shifts to the left as the pressure increases. The numerical simulation results validate that the impedance

curve can be an effective ‘probe’ to evaluate the working state of the rupture disc.

- (3) The resonant frequency of the PZT and rupture disc is stable when the inner pressure is low (≤ 1.2 MPa). However, as the loading pressure is larger than 1.2 MPa, the peak frequency shift to the left significantly. When the air pressure is close to its specified bursting pressure (1.9 MPa), the impedance curve is totally different, indicating that the inner pressure of the rupture disc increases significantly and it may be in a dangerous working state.
- (4) Three replacement matrices (RM_{RMSD} , RM_{MAPD} , and RM_{CCD}) were proposed and compared. The results show that replacement matrix based on the MPDA algorithm can quantitatively reveal the working states of the rupture disc.
- (5) For the in-site monitoring, the consequential effect of internal temperature and direct exposure to the environment should be investigated and temperature compensation technology should be considered. Experimental results show that, as the temperature increases, the resonance peak shifts to the left gradually. The resonant frequency shifts linearly with the temperature changes.

The study presented in this paper verifies that the EMI-based monitoring technique can estimate the working state of the rupture disc. The RM_{MAPD} can give a warning before the bursting of the rupture disc. By doing so, the quantitative evaluate the working states of the rupture disc can be achieved and the catastrophic overpressure of pressure vessels will be effectively prevented. The proposed methodology holds promising potential for the monitoring of rupture discs.

Author Contributions DC: conceptualization, methodology, formal analysis, investigation, writing—original draft, visualization. XX: investigation, writing—original draft, visualization. HX: formal analysis, investigation, writing—original draft. BG: formal analysis, investigation, writing—review and editing. LH: validation, writing—review and editing, supervision, funding acquisition. JY: writing—review and editing, supervision, project administration.

Funding Not applicable.

Availability of Data and Material Data and materials are available from the corresponding author upon reasonable request.

Declarations

Competing Interests The authors declare that they have no competing financial interests.

Ethical Approval and Consent to Participate Not applicable.

Consent for Publication Not applicable.

References

1. Bursting Disc Safety Devices. The Standardization Administration of China: Beijing. (2007)
2. The American society of mechanical engineers in ASME boiler and pressure vessel code III. Class 1 components: Division I-subsection NB. (1995)
3. Belevtsev, B.A., Freitag, V.A.: Pressure-relief valve with rupture disk. *Chem. Petrol. Eng.* **4**(3), 267–269 (1968)
4. Asahara, M., Saburi, T., Ando, T., Takahashi, Y., Miyasaka, T., Kubota, S.: Self-ignited flame behavior of high-pressure hydrogen release by rupture disk through a long tube. *Int. J. Hydrogen. Energ.* **46**(24), 13484–13500 (2021). <https://doi.org/10.1016/j.ijhydene.2021.01.097>
5. Somerday, B.P., Wiggans, K.T., Bradshaw, R.W.: Environment-assisted failure of alloy C-276 burst disks in a batch supercritical water oxidation reactor. *Eng. Fail. Anal.* **13**(1), 80–95 (2006). <https://doi.org/10.1016/j.engfailanal.2004.10.017>
6. Yang, C., Hui, H., Song, X., Huang, S.: Theoretical and experimental research on designed bursting pressure of ultrahigh pressure rupture disk. *J. Press. Vess. T.* **143**(3), 031301 (2021). <https://doi.org/10.1115/1.4048420>
7. Hu, Z., Yang, X., Wu, Z.: A study of bursting characteristics on hole-slot flat rupture discs (In Chinese). *J. Nanchang Univ. (Engineering & Technology)*. **15**(2), 14–21 (1993)
8. Jeong, J.Y., Lee, J., Yeom, S., Hong, S.C., Choi, W., Ryu, M., Kim, H., Lee, S.B.: A study on the grooving process of a cross-scored rupture disc. *Int. J. Precis. Eng. Man.* **13**(2), 219–227 (2012). <https://doi.org/10.1007/s12541-012-0027-1>
9. Sudha, C., Parameswaran, P., Kishore, S., Murthy, C.M., Rajan, M., Vijayalakshmi, M., Raghunathan, V.S.: Microstructure and deformation mode of a stainless steel rupture disc exposed to sodium-water reaction. *Mater. Charact.* **59**(8), 1088–1095 (2008)
10. Tang, J.Q., Geng, L.Y., Gong, J.M.: Analysis on bursting of rupture disc made by Inconel 600 Alloy. *Key. Eng. Mater.* **795**, 290–295 (2019). <https://doi.org/10.4028/www.scientific.net/KEM.795.290>
11. Hill, R.: A theory of the plastic bulging of a metal diaphragm by lateral pressure. *Philos. Mag.* **41**(322), 1133–1142 (1950)
12. Lake, G.F., Inglis, N.P.: The design and manufacture of bursting disks. *Proc. Inst. Mech. Eng.* **142**, 365–378 (1939). https://doi.org/10.1243/PIME_PROC_1939_142_026_02
13. Nesbitt, B.: Handbook of Valves and Actuators Valves Manual International. 1st Edition. (2006)
14. Moran, S.: An Applied Guide to Process and Plant Design. 2nd Edition. (2019)
15. Chen, D.D., Zhang, N.N., Huo, L.S., Song, G.B.: Full-range bolt preload monitoring with multi-resolution using the time shifts of the direct wave and coda waves. *Struct. Health. Monit. OnlineFirst* (2022). <https://doi.org/10.1177/14759217231158297>
16. Qu, C., Yi, T., Li, H.: Mode identification by eigensystem realization algorithm through virtual frequency response function. *Struct. Control. Health. Monit.* **26**(10), e2429 (2019). <https://doi.org/10.1002/stc.2429>
17. Yuan, S., Wang, H., Chen, J.: A PZT based on-line updated guided wave-Gaussian process method for crack evaluation. *IEEE. Sensor J.* **20**(15), 8204–8212 (2020). <https://doi.org/10.1109/JSEN.2019.2960408>
18. Qiu, L., Yuan, S.: On development of a multi-channel PZT array scanning system and its evaluating application on UAV wing box. *Sensor. Actuat. A. Phys.* **151**(2), 220–230 (2009). <https://doi.org/10.1016/j.sna.2009.02.032>
19. Patel, Y.R., Janušas, G., Palevicius, A., Palevicius, A., Lepšik, P.: Investigation of the hydrophobic properties of piezoelectric nanocomposites and applications in biomedical micro-hydraulic

- devices. *Mater. Tehnol.* **54**(3), 407–415 (2020). <https://doi.org/10.17222/mit.2019.249>
20. Bansal, T., Talakokula, V., Sathujoda, P.: A machine learning approach for predicting the electro-mechanical impedance data of blended RC structures subjected to chloride laden environment. *Smart. Mater. Struct.* **31**(1), 015036 (2021)
 21. Chen, H., Xu, B., Wang, J., Luan, L., Zhou, T., Nie, X., Mo, Y.: Interfacial debonding detection for rectangular CFST using the MASW method and its physical mechanism analysis at the meso-level. *Sensors.* **19**(12), 2778 (2019). <https://doi.org/10.3390/s19122778>
 22. Gao, W., Huo, L., Li, H., Song, G.: An embedded tubular PZT transducer based damage imaging method for two-dimensional concrete structures. *IEEE. Access.* **6**, 30100–30109 (2018). <https://doi.org/10.1109/ACCESS.2018.2843788>
 23. Wang, J., Li, W., Luo, W., Wu, J., Lan, C.: Modeling and experimental validation of a quantitative bar-type corrosion measuring probe using piezoelectric stack and electromechanical impedance technique. *Measurement* **188**, 110546 (2022). <https://doi.org/10.1016/j.measurement.2021.110546>
 24. Chen, D.D., Shen, Z.H., Fu, R.L., Yuan, B., Huo, L.S.: Coda wave interferometry-based very early stage bolt looseness monitoring using a single piezoceramic transducer. *Smart. Mater. Struct.* **31**(3), 035030 (2022). <https://doi.org/10.1088/1361-665X/ac5128>
 25. Chen, D.D., Huo, L.S., Song, G.B.: High resolution bolt preload looseness monitoring using Coda Wave Interferometry. *Struct. Health. Monit.* **21**(5), 1959–1972 (2022). <https://doi.org/10.1177/14759217211063420>
 26. Hei, C., Luo, M., Gong, P., Song, G.: Quantitative evaluation of bolt connection using a single piezoceramic transducer and ultrasonic coda wave energy with the consideration of the piezoceramic aging effect. *Smart. Mater. Struct.* **29**(2), 027001 (2019). <https://doi.org/10.1088/1361-665X/ab6076>
 27. Kong, Q.Z., Rachel, R., Pedro, S., Mo, Y.: Cyclic crack monitoring of a reinforced concrete column under simulated pseudo-dynamic loading using Piezoceramic-based smart aggregates. *Appl. Sci.* **6**(11), 341–341 (2016). <https://doi.org/10.3390/app6110341>
 28. Feng, Q., Kong, Q.Z., Tan, J., Song, G.B.: Grouting compactness monitoring of concrete-filled steel tube arch bridge model using piezoceramic-based transducers. *Smart. Struct. Syst.* **20**(2), 175–180 (2017). <https://doi.org/10.12989/sss.2017.20.2.175>
 29. Wang, T., Liu, S.P., Shao, J.H., Li, Y.R.: Health monitoring of bolted joints using the time reversal method and piezoelectric transducers. *Smart. Mater. Struct.* **25**(2), 025010 (2016). <https://doi.org/10.1088/1361-665X/aa6e93>
 30. Li, W., Wang, J., Liu, T., Luo, M.: Electromechanical impedance instrumented circular piezoelectric-metal transducer for corrosion monitoring: modeling and validation. *Smart. Mater. Struct.* **29**, 035008 (2020). <https://doi.org/10.1088/1361-665X/ab675c>
 31. Huo, L., Wang, F., Li, H., Song, G.: A fractal contact theory based model for bolted connection looseness monitoring using piezoceramic transducers. *Smart. Mater. Struct.* **26**(10), 104010 (2017). <https://doi.org/10.1088/1361-665X/aa6e93>
 32. Zhang, H., Wang, L.L., Li, J.J., Kang, F.: Embedded PZT aggregates for monitoring crack growth and predicting surface crack in reinforced concrete beam. *Constr. Build. Mater.* **364**, 129979 (2023). <https://doi.org/10.1016/j.conbuildmat.2022.129979>
 33. Fu, R.L., Mao, R.W., Yuan, B., Chen, D.D., Huo, L.S.: Multi-resolution bolt preload monitoring based on the acoustoelastic effect of ultrasonic guided waves. *Smart. Mater. Syst.* **30**(5), 513–520 (2022). <https://doi.org/10.12989/sss.2022.30.5.513>
 34. He, S., Zhang, G., Song, G.: Design of a networking stress wave communication method along pipelines. *Mech. Syst. Signal. Pr.* **163**, 108192 (2022). <https://doi.org/10.1016/j.ymssp.2021.108192>
 35. Li, W., Liu, T., Zou, D., Wang, J., Yi, T.: PZT based smart corrosion coupon using electromechanical impedance. *Mech. Syst. Signal. Pr.* **129**, 455–469 (2019). <https://doi.org/10.1016/j.ymssp.2019.04.049>
 36. Liang, C., Sun, F.P., Rogers, C.A.: An impedance method for dynamic analysis of active material systems. *J. Intel. Mat. Syst. Str.* **116**(1), 120–128 (1994). <https://doi.org/10.1115/1.2930387>
 37. Giurgiutiu, V., Reynolds, A., Rogers, C.A.: Experimental investigation of E/M impedance health monitoring for spot-welded structural joints. *J. Intel. Mat. Syst. Str.* **10**(10), 802–812 (1999). <https://doi.org/10.1106/N0J5-6UJ2-WIGV-Q8MC>
 38. Chen, D., Huo, L., Song, G.: EMI based multi-bolt looseness detection using series/parallel multi-sensing technique. *Smart. Struct. Syst.* **25**(4), 423–432 (2020). <https://doi.org/10.12989/sss.2020.25.4.423>
 39. Kim, J.T., Nguyen, K.D., Park, J.H.: Wireless impedance sensor node and interface washer for damage monitoring in structural connections. *Adv. Struct. Eng.* **15**(6), 871–885 (2012). <https://doi.org/10.1260/1369-4332.15.6.871>
 40. Na, W., Baek, J.: Impedance-based non-destructive testing method combined with unmanned aerial vehicle for structural health monitoring of civil infrastructures. *Appl. Sci.* **7**(1), 15 (2016). <https://doi.org/10.3390/app7010015>
 41. Giurgiutiu, V., Rogers, C.A.: Recent advancements in the electromechanical (E/M) impedance method for structural health monitoring and NDE. *Proceedings of SPIE - The International Society for Optical Engineering.* 3329 (1998)
 42. Liang, Y.B., Li, D.S., Parvasi, S.M., Song, G.B.: Load monitoring of pin-connected structures using piezoelectric impedance measurement. *Smart. Mater. Struct.* **25**(10), 105011 (2016)
 43. Lim, Y.Y., Soh, C.K.: Effect of varying axial load under fixed boundary condition on admittance signatures of electromechanical impedance technique. *J. Intel. Mat. Syst. Str.* **23**(7), 815–826 (2012). <https://doi.org/10.1177/1045389X12437888>
 44. Park, G., Sohn, H., Farrar, C.R., Inman, D.J.: Overview of piezoelectric impedance-based health monitoring and path forward. *Shock. Vib.* **35**(6), 451–464 (2003). <https://doi.org/10.1177/05831024030356001>
 45. Park, S., Ahmad, S., Yun, C.B., Roh, Y.: Multiple crack detection of concrete structures using impedance-based structural health monitoring techniques. *Exp. Mech.* **46**(5), 609–618 (2006). <https://doi.org/10.1007/s11340-006-8734-0>
 46. Stepanov, A.P.: Rupture disks. *Chem. Petrol. Eng.* **4**, 46–47 (1976). <https://doi.org/10.1007/BF01161331>
 47. Li, S.C.: Burst pressure calculation for grooved explosion proof membrane (in Chinese). *Petro-chem. Eq. Technol.* **3**, 49–54 (1986)
 48. Lin, S.Y.: Analysis on the resonance frequency of a thin piezoelectric ceramic disk in radial vibration. *J. Shaanxi Norm. Univ. (Natural Science Edition)* **34**(1), 27–31 (2006). <https://doi.org/10.15983/j.cnki.jsnu.2006.01.008>
 49. Guo, B., Chen, D.D., Huo, L.S., Song, G.B.: Monitoring of grouting compactness in tendon duct using multi-sensing Electro-mechanical impedance method. *Appl. Sci.* (2020). <https://doi.org/10.3390/app10062018>
 50. Tseng, K.K.H., Naidu, A.S.K.: Non-parametric damage detection and characterization using smart piezoceramic material. *Smart. Mater. Struct.* **11**(3), 317 (2002). <https://doi.org/10.1088/0964-1726/11/3/301>
 51. Zhao, S., Fan, S.L., Chen, J.Y.: Quantitative assessment of the concrete gravity dam damage under earthquake excitation using electro-mechanical impedance measurements. *Eng. Struct.* **191**, 162–178 (2019). <https://doi.org/10.1016/j.engstruct.2019.04.061>
 52. Sun, F.P., Chaudhry, Z., Liang, C., Rogers, C.A.: Truss structure integrity identification using PZT sensor-actuator. *J. Intel. Mat. Syst. Str.* **6**(1), 134–139 (1995). <https://doi.org/10.1177/1045389X9500600117>

53. Sirohi, J., Chopra, I.: Fundamental understanding of piezoelectric strain sensors. *J. Intel. Mat. Syst. Str.* **11**(4), 246–257 (2000). <https://doi.org/10.1106/8BFB-GC8P-XQ47-YCQ0>
54. Park, S., Kim, J.W., Lee, C., Park, S.K.: Impedance-based wireless debonding condition monitoring of CFRP laminated concrete structures. *Ndt&E. Int.* **44**(2), 232–238 (2011). <https://doi.org/10.1016/j.ndteint.2010.10.006>
55. Grisso, B.L., Inman, D.J.: Autonomous hardware development for impedance-based structural health monitoring. *Smart. Struct. Syst.* **4**(3), 305–318 (2008). <https://doi.org/10.12989/sss.2008.4.3.305>
56. Nguyen, K.D., Kim, J.T.: Smart PZT-interface for wireless impedance-based prestress-loss monitoring in tendon-anchorage connection. *Smart. Struct. Syst.* **9**(6), 489–504 (2012). <https://doi.org/10.12989/sss.2012.9.6.489>

Publisher's Note Springer Nature remains neutral with regard to jurisdictional claims in published maps and institutional affiliations.

Springer Nature or its licensor (e.g. a society or other partner) holds exclusive rights to this article under a publishing agreement with the author(s) or other rightsholder(s); author self-archiving of the accepted manuscript version of this article is solely governed by the terms of such publishing agreement and applicable law.